Energetically deposited cluster assembly of metallic glasses

Syamal Praneeth Chilakalapudi[a,d,*], Shyam Katnagallu[a,b], Abhishek Sarkar[a,d], Penghui Cao[c], Wolfgang Wenzel[a], Horst Hahn[a,c,d,*]

[a] *Institute of Nanotechnology, Karlsruhe Institute of Technology, Karlsruhe, Germany*
[b] *Max-Planck-Institut für Eisenforschung GmbH, Düsseldorf, Germany*
[c] *Department of Materials Science and Engineering, University of California Irvine, Irvine, USA*
[d] *KIT–TUD Joint Research Laboratory Nanomaterials, Technische Universität Darmstadt, Darmstadt, Germany*

Keywords:
Cluster-assembled glass
Metallic glasses
Amorphous structure tailoring
Molecular dynamics

A B S T R A C T

Metallic glasses, prepared by rapid quenching and ball milling, have been studied extensively for decades. Nevertheless, they are not as well understood as crystalline materials in terms of structure and local atomic packing. The assembly of amorphous nanoclusters by energetic deposition has recently been shown as an alternative route to synthesize amorphous films. Furthermore, the local atomic structures of these cluster-assembled films were found to be different from that of the rapidly quenched metallic glass of the same composition. However, the underlying mechanisms, which result in these novel structures of the cluster-assembled films are hitherto unknown. An atomistic molecular dynamics study of the formation of $Cu_{50}Zr_{50}$ cluster-assembled metallic glass films is presented. Two amorphous phases are identified: one in the cores of the clusters, and the other in the continuous network of interfaces formed amongst the clusters. These two phases are chemically distinct from one other and also different from the rapidly quenched metallic glasses. An increased short-range order is observed in the interfaces, while the cores occupy lower energy states. The present results further demonstrate that the amorphous short- and medium-range orders of cluster-assembled glasses not only differ from rapidly quenched glass of the same macroscopic composition, but can be tailored by the variation of the deposition energy.

1. Introduction

Rapid-quenching from the melt (RQ) and ball milling of elemental or alloy powders (BM) have been the well-established methods for the preparation of metallic glasses (MG) for decades [1,2]. Generally, it has been observed that the properties of MGs, prepared by RQ or BM, vary substantially depending on the preparation parameters. With subsequent heat treatments, well-defined amorphous structures–typically characterized by a homogeneous distribution of the constituent elements–with reproducible properties can be established. Since their discovery by the Klement et al. [1], the structure and properties of MGs have been studied extensively for a large variety of systems and compositions, leading to the observation of many favorable structural properties and functional applications [3–6].

Some 30 years back, motivated by the early work on nanocrystalline materials produced via compaction of nanopowders, Gleiter and coworkers obtained a new class of metallic glasses called nanoglasses (NG) by the compaction of amorphous PdFeSi nanoparticles [7,8]. This initial research and several follow-up publications [8–14] showed that these NGs, prepared by a bottom-up approach, exhibit additional structural features not present in MGs prepared by RQ and BM, which are interpreted as interfaces between the nanoparticles [7]. The structural model resembles that of nanocrystalline materials, i.e., cores embedded in an interfacial network with the difference that NGs exhibit a fully amorphous structure, i.e., both cores and interfaces are amorphous [9,15–18]. Furthermore, the mechanical and physical properties of the NGs differ from those obtained for the MGs of identical compositions [15,19,20].

More recently, it has been demonstrated that MGs can also be produced by the energetic deposition of small clusters, in the size range of 10–2000 atoms per cluster, onto a substrate [21–24]. These materials are called cluster-assembled metallic glasses (CAMG). In fact, the size range of the building blocks, i.e., clusters, of CAMGs is substantially smaller than the nanoparticles,

* Corresponding authors at: Institute of Nanotechnology, Karlsruhe Institute of Technology, Karlsruhe, Germany.
E-mail addresses: sp.chila@kit.edu (S.P. Chilakalapudi), horst.hahn@kit.edu (H. Hahn).

i.e., the building blocks of NGs. Moreover, the CAMGs are produced by the energetic impact of clusters onto a substrate, instead of mechanical compaction. Hence, the resulting two families of metallic glasses, NGs and CAMGs, are expected to exhibit different structural features, which are in turn expected to differ from those of MGs. The opportunities to modify the amorphous structure, and consequently the properties by the novel preparation methods motivates the research on NGs and the novel CAMGs. In a first report for CAMGs prepared from the smallest clusters in the size range of 10–16 atoms each, it was shown by synchrotron-based diffraction techniques that the deposition of these clusters results in an amorphous film, without further exploration of the structural details [21,22]. For CAMGs, assembled by energetic impact of $Fe_{80}Sc_{20}$ clusters with 800 atoms per cluster on average, it has been observed that the structure, characterized by the structural motifs and the magnetic Curie transition temperature, T_C, can both be controlled by the impact energy of the clusters onto the substrate [23,24]. However, a deeper understanding of CAMGs is still needed.

For MGs and NGs, several structural models which support experiments in the CuZr and PdSi binary systems have been published [16–18,25–29], some of which will be used as the base for the discussions in later sections. In contrast, the knowledge of the atomic structure of CAMGs is limited to the extended X-ray absorption fine structure (EXAFS) study of the $Fe_{80}Sc_{20}$ CAMG [24]. Attempts at exploring structures of CAMGs even with advanced Transmission Electron Microscope (TEM) studies, or Atom-probe Tomography (APT) characterization are constrained by experimental challenges and even so would fail at imparting a complete structural description of CAMGs.

The objective of the present study is to employ molecular dynamics simulations to provide predictive insights in the structure of CAMGs, in particular on the role of the processing parameters in the synthesis of CAMGs, with a special emphasis on how the deposition energy (also referred as impact energy) affects both the structure and packing of the CAMGs in comparison to both MGs and NGs. With the intention to connect to various previous studies on MGs and NGs, and also due to availability of a molecular dynamics potential, we have chosen to model CuZr CAMGs.

2. Methods

Atomistic molecular dynamics (MD) simulations of binary $Cu_{50}Zr_{50}$ glasses in the different states MG, NG and CAMG have been performed using the LAMMPS code [30,31]. A semi-empirical potential developed with data from $Cu_{46}Zr_{54}$ alloys [32], based on the Embedded-Atom Method (EAM) proposed by Daw et al. [33], was used to model the Cu-Zr interactions. The $Cu_{50}Zr_{50}$ MGs were simulated by quenching from the liquid state to 50 K. The liquid state was simulated by equilibrating an equimolar mixture of Cu and Zr atoms placed at random coordinates at 2000 K for 2 ns. The quenching to the glassy state was performed at zero pressure at three cooling rates of 10^{10}, 10^{12} and 10^{14} K/s. The system temperature and pressure were controlled by using a Nosé-Hoover thermostat (NPT in LAMMPS). The MGs will be referred to by the quench rate: for instance, an MG quenched at 10^{10} K/s will be referred to as a 10^{10} K/s MG, and so on. For the case of the 10^{10} K/s MG, which requires a much longer and computationally expensive simulation, a sample of ~16,000 atoms was chosen, and replicated in all three dimensions, resulting in a larger sample of ~150,000 atoms in total. For the 10^{12} K/s and 10^{14} K/s MGs, in which the simulation costs are less, the larger samples of ~150,000 atoms were prepared directly. Periodic boundary conditions were used in all three directions, and a time step of 1 fs was chosen for all simulations. After quenching, the metallic glasses were equilibrated for 2 ns at 50 K. Analysis and visualizations were made using custom Python scripts, which utilized the OVITO API [34] and the Pizza.py toolkits [35]. Additional details of the simulations of the NGs and CAMGs are given in the next section.

3. Results and discussion

3.1. Cluster synthesis

In the present work, the structure of CAMGs with a specific size of the clusters as a function of impact energy is studied using MD simulations. The structure of CAMGs will be compared to MGs prepared by RQ. The CAMGs structure will also be compared to NGs prepared by compaction process using the same original clusters as for the simulation of the CAMGs. The clusters, NGs, and CAMGs discussed in this section and the following sections up until Section 3.9, are limited to the 10^{10} K/s $Cu_{50}Zr_{50}$-MG.

Consequently, in a first step, a free-standing cluster was prepared by cutting a sphere of 3 nm diameter (with ~800 atoms) from a 10^{10} K/s $Cu_{50}Zr_{50}$-MG held at 50 K temperature. The resulting cluster was found to be approximately at a $Cu_{50}Zr_{50}$ composition (with a ~1% deviation). As reported earlier by Adjaoud and Albe [29], any cluster develops surface stresses immediately after cutting. The slow kinetics at 50 K prevent the atoms from relaxing to their lowest energetic state. Therefore, a short-time increase of the temperature of the cluster, which increases the mobility of the atoms, allows to obtain a configuration similar to a cluster synthesized in a real experiment by inert-gas condensation (IGC). Thus, the protocol developed in Ref. [29], viz., heating the cluster to 1000 K, i.e., beyond the glass-transition temperature (T_g), followed by cooling it back to 50 K, was employed. Both the heating and cooling was performed at a rate of 2.5×10^{12} K/s. Although T_g is crossed in the simulation, crystallization is avoided (see Section 3.5) due to the short heating time; sufficient diffusion occurs over the short distances to establish a concentration profile in the cluster. In addition, the cluster was equilibrated for 2 ns both after the cutting and after the heat treatment. The heat treatment and its effect on the structure of the cluster is visualized in Fig. 1a for a cluster derived from the 10^{10} K/s MG. The evolution of the Cu composition in a 0.2 nm thick shell at a radius of 1.3 nm is shown. The definition of a shell region is independently ascertained by the difference in composition, determined by a radial compositional analysis (Section S1, Supplementary Information). Up to a time $t = 2$ ns, when the cluster is equilibrated at 50 K, the Cu composition remains constant. The heating and cooling spike of the cluster between $t = 2$ ns and $t = \sim 3$ ns results in a sharp increase of the Cu-concentration in the outer shell compared to the bulk composition, eventually leveling off at about 56.48 at.%. In the remaining core volume, the Cu concentration decreases to 44.59 at.%. While the overall composition of the 3 nm cluster remains unchanged, two distinct regions are seen in the equilibrated cluster-a core region with a lower Cu concentration, and a shell region with a substantially higher Cu concentration. The inset in Fig. 1a depicts the core (colored magenta) and shell (colored yellow) regions of the cluster. As in other reports [15,22,29], Cu-atoms segregate towards the cluster surface—increasing the Cu concentration by 9 at.% as compared to the initial homogeneous composition, while the Zr-atoms are enriched in the core. This compositional variation on the length scale of the cluster size is carried over to the interfacial regions between clusters upon compaction or energetic impact. From previous studies it is known that such chemical heterogeneities in compacted NGs on the nanometer length scale stabilize the amorphous structure [29].

A heat treatment as just described for the single cluster can also modify the metastable state and structure of a MG. Therefore, the as-prepared MG sample, i.e., quenched directly from the liquid phase, was subjected to a heat treatment identical to the one used for the single cluster to determine the changes in the

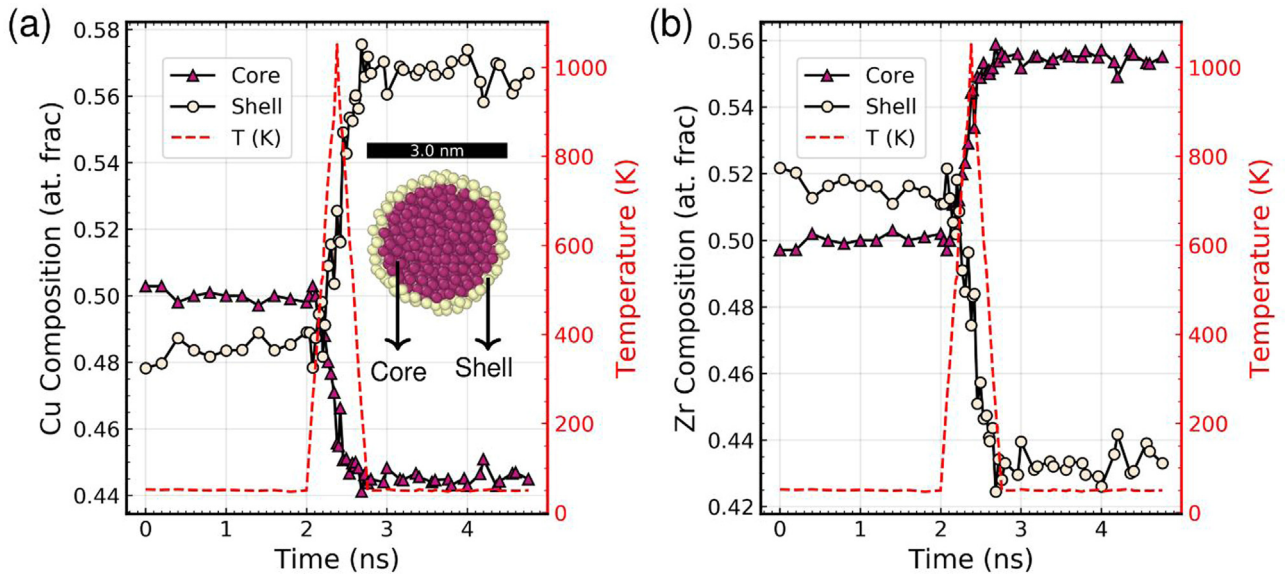

Fig. 1. Variation of composition of a 3 nm $Cu_{50}Zr_{50}$ cluster during a heat spike. In (a), the redistribution of copper atoms by diffusion during the heat spike is seen, leading to an enrichment of Cu atoms in a shell (the core-shell structure is illustrated in the inset) of 0.2 nm thickness. Correspondingly, in (b) a concurrent decrease of the Zr concentration is seen in the shell. Consequently, the Cu concentration decreases in the core and increases in the shell as the cluster is heated up to and beyond T_g.

structure of the MG sample. In addition to the as-prepared MG, the heat-treated metallic glass (MG_ht) serves as an additional reference structure for the NGs and CAMGs prepared by compaction and energetic impact, respectively. In the following discussion up until Section 3.9, the NGs and CAMGs derived from the cluster made only from the 10^{10} K/s MG are considered.

3.2. Cluster deposition: CAMGs

3.2.1. Single cluster deposition

In order to understand the role of the impact energy on the cluster deposition and to identify the range of impact energy of interest for the preparation of CAMGs, the deposition of a single cluster on a substrate was initially studied. The single $Cu_{50}Zr_{50}$ cluster, 3 nm in diameter— prepared as described above—was deposited at various energies ranging from 6 to 6000 meV per atom. These simulation conditions represent closely the experimental conditions in the cluster ion beam deposition (CIBD) experiments, in terms of cluster size and range of impact energies [23,24]. In the CIBD experiments, CuZr clusters are generated as charged cluster-ions and then guided as a particle-beam towards the substrate using an electric field. The strength of the said electric field determines the impact energy of the cluster ions onto the substrate. In the present simulation, a classical momentum was given to the cluster to mimic the cluster-acceleration in the experiments, when they pass through the electric field. Furthermore, in the experimental CIBD set-up, the substrate is electrically grounded to prevent any charge buildup on the surface [36]. Therefore, the deposition process can be modeled with classical molecular dynamics without taking electrodynamics into account. In terms of the thermodynamics, the cluster is modeled as a closed system (micro-canonical ensemble). A simplification, which was made in the MD simulations, is the replacement of the oxidized Si-substrate used in the experiments [23,24] with an amorphous $Cu_{50}Zr_{50}$ substrate, equilibrated for 2 ns. A layered thermal model with the following configuration was used to represent the substrate: 1. the top layer (modeled as a micro-canonical ensemble) serving as a buffer between the clusters and the substrate, 2. the middle layer being coupled with a heat sink, using a Nosé-Hoover Thermostat to hold the substrate temperature at 50 K, and 3. the bottom layer, with atoms held fixed to mimic the rigidity of the substrate. The buffer and thermostatted layers had a minimum thickness of two-atom layers (see Fig. S2 in Supplementary Information). It is important to note that all three layers are essential to model the substrate. Without the first layer, the deposited atoms would immediately quench onto the substrate. The second layer accounts for temperature control, the lack of which would have led to a thermally unstable (explosive) substrate caused by its inability to expel sufficient amounts of energy from the system. Furthermore, without the third layer, the substrate would have no mechanical rigidity, and the clusters will simply pass through the substrate at higher energies. The layer model was configured in accordance with previous MD thin film studies [37–39]. For the case of the single cluster depositions, a semi-hemispherical layout was utilized for the thermostatted layer to account for a spherical shockwave that passes through the substrate. For these single cluster depositions, the substrate length and width were chosen to be 6 nm: two times as wide as the cluster diameter.

The thickness of the first two layers (buffer and thermostatted layers) can affect the heat absorption and also the hardness of the substrate. Consequently, the dissipation of the energy introduced to the film-substrate system by the cluster deposition is influenced by the specific design of the layers. For the present substrate model, the deposition of a single cluster was inspected at large timescales, and it was found that the simulation converges approx. 2 ns after the cluster deposition (see Fig. S4 in Supplementary Information). Fig. 2 shows the cross-sections of the clusters deposited at various energies in the YZ plane parallel to the deposition axis, 2 ns after deposition. The atoms colored in yellow and magenta, belong to the shell and core atoms of the cluster prior to deposition, respectively. No distinction is made in this color code for the constituent elements. All substrate atoms are colored in black. Clearly, the morphology of the cluster after impact varies with deposition energy. In the energy range of 6–60 meV/atom, the cluster is in a soft-landing state. In this regime, it is observed that even for the lowest deposition energy of 6 meV/atom the cluster loses the original shape of the free cluster, which was almost perfectly spherical. This change of shape is attributed to a partial

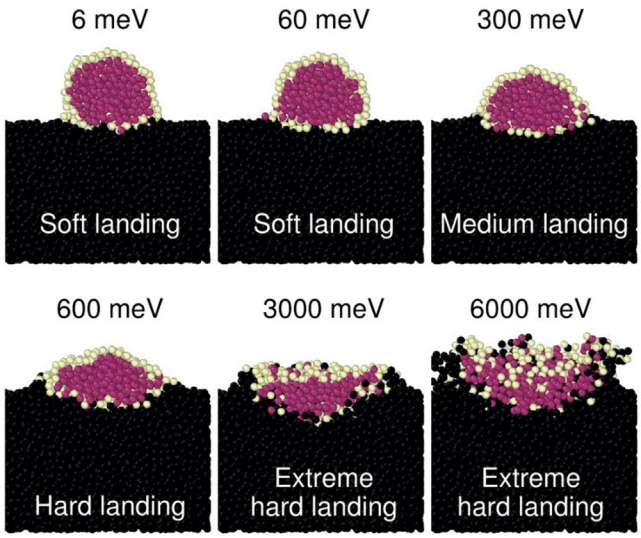

Fig. 2. Single cluster deposited states. The cross sections of snapshots of the clusters, 2 ns after the simulated deposition at various per-atom energies ranging from 6 to 6000 meV/atom are shown, with categories of soft, medium, hard and extreme hard landing indicated. The core and shell atoms are marked in magenta and yellow colors, respectively. This is the same color scheme as used in Fig. 1.

wetting due to the cohesive forces at the surface between the cluster and the substrate. No noticeable difference in the final shapes is observed for the cases of 6 meV/atom and 60 meV/atom impact energy. As more drastic changes of the cluster shape are observed at higher impact energies, the deposition energy of 60 meV/atom was chosen to be the upper limit for the soft-landed state.

For all simulated cluster impacts, it is observed in Fig. 2 that the impact energy clearly influences the final states of the shell atoms in the clusters. The shell region stays intact at energies below 600 meV/atom. However, for impact energies $\geq$ 600 meV/atom, i.e., in the hard-landed state, the distortion of the cluster increases continuously with increasing impact energy. The deposition at 300 meV/atom energy is then defined as the medium-landed state. The separation between soft, medium and hard landing is assigned arbitrarily. However, these distinctions allow us to understand the broad energy regimes in which the CAMGs retain or lose the signatures of the originally free clusters. In the soft-landed state, the clusters in the CAMGs can be expected to remain mostly spherical. At the higher energies, in the medium-landed state, the cluster is expected to deform further. In the hard-landing state, not only will the cluster be deformed, but the inter-diffusion of the core-shell atoms in the cluster becomes significant. The deformation of clusters is quantified in Section S2 of the Supplementary Information.

The cluster is also observed to lose its spherical morphology at higher impact energies. At energies $\geq$ 600 meV, i.e., hard and extreme hard landing, the cluster embeds itself into the substrate during impact. The cluster adopts a concave shape on the substrate. With increasing impact energy, the cluster deforms more and embeds deeper into the substrate. In the context of formation of CAMG films, i.e., when multiple clusters are deposited over each other layer-by-layer, intermixing between clusters is expected at the higher impact energies. Based on the results of the single cluster deposition, impact energies between 60 and 600 meV/atom were chosen to study the formation of CAMG films. In the following section, as part of a first analysis, the changes of the core-shell structures during multiple cluster deposition will be considered.

3.2.2. Multiple cluster deposition

Following the simulations of deposition of single clusters, the deposition of multiple clusters to form CAMG films was modeled. A large $Cu_{50}Zr_{50}$ substrate of dimensions 25 nm $\times$ 25 nm $\times$ 3 nm, consisting of about ~75,000 atoms was chosen. As described in the previous section, the substrate model is tri-layered, but with flat substrate layers (see Fig. S6 in Supplementary Information). Both the buffer and thermostatted-layer are set to an initial temperature of 50 K. As an initial test, single cluster depositions on this larger substrate were also found to relax after 2 ns (see Fig. S7a in Supplementary Information). Therefore, each cluster is allowed to relax for 2 ns after deposition before another cluster is deposited next or on top to it. In the CAMG experiment [24], the clusters are polydisperse in nature, with a log-normal size distribution, while in the present simulations, however, each cluster is chosen to be of the same size. In addition, each cluster is allowed to rotate by three random Euler angles before deposition to ensure a random configuration in the CAMG film samples. The simulation was performed with periodic boundary conditions in the XY plane. The deposition of the clusters on the substrate at random locations in the XY plane resulted in the formation of pillars, thus shadowing certain regions of the film and leading to porous films (see Fig. S7b in Supplementary Information). The growth of the porous film bore resemblance to previous statistical studies on ballistic deposition [40]. Although such pores may occur in the experiments, here a model was used to maximize inter-cluster interactions and to avoid formation of pores. An absence of surface effects from the pore formation and an increase of cluster-cluster interfaces is desirable to study the effects of interfaces in CAMGs. In order to achieve a higher packing density, the clusters were deposited in a hexagonal close-packed (HCP) arrangement onto the substrate (see Fig. 3b).

3.3. Cluster compaction: nanoglasses

One of the aims of this study is to compare CAMGs to metallic glasses prepared by mechanical compaction, i.e., NGs. The results of simulations of CAMGs and NGs using the same clusters as building blocks allows a comparison of the different processing techniques, compaction for NGs and energetic impact for CAMGs. Furthermore, the structure of simulated NGs prepared by compaction of clusters in the size range of 800 atoms has not been reported. For the simulation of the cold compaction, the clusters were inserted in a simulation box and compacted at 50 K temperature under 5 GPa pressure to yield a NG of ~300,000 atoms. In previous works, the compaction of NGs was modeled by inserting the clusters at random positions before compaction [17,41] as this method closely resembles the actual experiments conducted to obtain NGs. However, in this study, the clusters were inserted in a HCP arrangement prior to compaction in order to resemble the arrangement used for the CAMGs. Such a regular cluster arrangement to make NGs has been employed in previous works as well [16,18,42,43]. Once the sample was compacted at 50 K temperature and equilibrated, it was unloaded for 0.2 ns and then equilibrated again for another 2 ns. In the NG-sample prepared in this way no pores were present, when examined using a surface mesh with a probe sphere radius of 3 Å [34,44].

3.4. Identification of cores and interfaces in CAMGs

The deposition of multiple clusters, with clusters derived from 10^{10} K/s $Cu_{50}Zr_{50}$ MG, was simulated at 60 meV/atom, 300 meV/atom, 600 meV/atom impact energies to mimic the soft, medium, and hard-landing in the CAMG film samples, respectively. Additionally, a deposition at extreme energetic conditions was simulated at the impact energy of 6000 meV/atom. The HCP arrangement for each impact energy was achieved in the following manner: before each new cluster was deposited, the clusters that were already present in its neighborhood were relaxed for at least 2 ns.

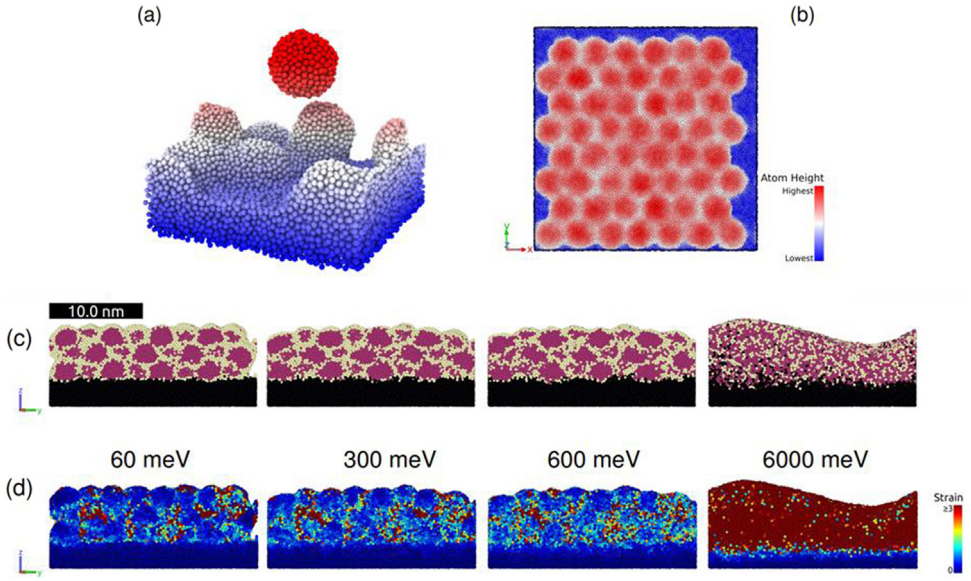

Fig. 3. Deposition of CAMG films: (a) A depiction of the deposition of a cluster onto the substrate and (b) a top view of the clusters deposited in a HCP arrangement (color coded by the atom height in the deposition axis). (c) A vertical cross-section of the deposited films at 60, 300, 600, and 6000 meV/atom energies, with cluster-core atoms in magenta, and cluster-shell atoms in yellow. The substrate atoms are colored in black. The shell atoms form a network of interfaces across the film at least up to 600 meV/atom deposition energy. (d) When color coded with von Mises shear strain, the interfacial atoms correlate with the higher strained atoms.

Every simulated CAMG had three layers of such cluster depositions, with ∼50 clusters in each layer. The deposition sequence and the processes occurring during impact can be followed in the Supplementary Video V1, which shows the simulation of the deposition of CAMGs in comparison to that of the compaction in the NG processing.

Fig. 3c shows cross-sections of the films, similar to Fig. 2, after equilibrating the sample for 2 ns after the deposition of the last cluster. The yellow and magenta color coding denotes the shell and core atoms of the clusters prior to deposition, similar to Figs. 1 and 2. No evidence for porosity is observed even for the soft-landing sample (60 meV/atom case) by evaluating a surface mesh with a probe sphere radius of 2.4 Å [34,44]. At the lowest impact energy of 60 meV/atom, it is observed that, like in Fig. 2, the deposited clusters mostly retain their initial sphericity. The cluster sphericity is progressively lost with increasing deposition energy. Next, it should be noted that the first layer of clusters has resided on the substrate for at least 24 ns (using the deposition protocol described) by the time the final layer is deposited. Nevertheless, the interdiffusion of the core and shell atoms is quite low for deposition energies even up to 600 meV/atom. In the energy range of 60–600 meV/atom, the shell atoms, i.e., the former surface atoms of the free cluster prior to deposition, are forming a distinct interconnected network, which can be interpreted as atomically thin interfacial regions between the cores of the clusters. The former shell atoms (colored yellow as mentioned above) of the clusters are hence defined to constitute the cluster-cluster interfaces. At the impact energy of 6000 meV/atom the interfacial regions vanish completely. Additionally, this film shows significant atomic intermixing between the substrate and the film (see Fig. 3, visualizing the black substrate atoms found in the film, and magenta and yellow atoms from the deposited film embedded in the substrate). For the case of the 6000 meV/atom energy, it is estimated that 8% of the atoms originally in the film are mixed into the substrate, whereas for the case of the 600 meV/atom impact energy this value is about 1.7%. Similarly, the mixing of the substrate atoms diffusing into the film sample was also ascertained, by tracking the substrate atoms in the final deposited films. The mixing of the substrate atoms into the film has been estimated to be 6% for 600 meV/atom case, and is 16% for the 6000 meV/atom case. For both the film and substrate atoms, the diffusion into the neighboring medium is higher at higher impaction energies.

Up to now, the locations of the atoms initially at the surfaces of the clusters prior to deposition, have been followed (using the magenta and yellow color scheme for the core and shell atoms, respectively) to determine the interfacial regions in the samples prepared with impact energies in the range below 600 meV/atom. This approach does not provide any information on the energetic state of the atoms in the CAMGs or on the local environments in the cores and interfaces. In a first step towards a more detailed analysis, the von Mises shear strain for each of the CAMG atoms was determined [17,18,42,44,45]. A cut-off radius of 3.8 Å was chosen to compute the strain tensor. In Fig. 3d, the high strain regions can be clearly correlated to the interfacial network shown in Fig. 3c for all impact energies below 600 meV/atom. Only for the highest impact energy, no sign for the presence of interfaces can be found, similar to the observation in Fig. 3c. The correlation observed for CAMGs is consistent with Gleiter's original definition of interfaces [46] in NGs, in which the interfaces were assumed to be regions of distorted and sheared coordination among adjacent clusters. The strain maps in Fig. 3d confirm that an interfacial structure is formed and is retained in the range of 60–600 meV/atom impact energies. Upon inspection of the simulation snapshots in OVITO, the cores and interfaces in the CAMG film samples made by soft-to-high landing deposition are found to reflect a chemical heterogeneity similar to what was originally present in the free clusters prior to deposition (described in Fig. 1a), with the Cu concentration of ∼46 at.% in the cores, and ∼55 at.% in the interfacial regions. The overall composition of the CAMG films are found to be $Cu_{50}Zr_{50}$ (with 1% deviation), same as of the original clusters. The atoms in the CAMG film sample for the extreme hard-landing case of 6000 meV/atom indicate a loss of core and interface structure, and in this manner resembling the MGs obtained by RQ. This loss of core-interface structure, also observed from von Mises local strains is indicative of a high deviation of atoms from their as-deposited positions in the clusters, likely due to local melting and resolidification near deposition sites. It should be mentioned that the processing of NGs and CAMGs seems to differ in one aspect: at

the harshest conditions, i.e., at the extreme hard-landing case for CAMGs and at the highest pressures for NGs, the final structures are different. In NGs, the interfacial regions continue to exist even at the highest pressures, while the interfacial regions disappear in CAMGs at the extreme hard-landing. This most likely is caused by the differences between the compaction and deposition processes. While the cold compaction shears the entire arrangement of clusters together, the sequential deposition of the clusters along with local heating due to the inelastic collision may result in the dissolution of the cluster structure. Therefore, the energetic impact of clusters is considered as a novel process leading to metallic glasses. CAMGs also contain interfacial regions with a modified structure, which differs from that of RQ MGs and NGs prepared by high pressure compaction. However, it is not clear if the structural details of the interfacial regions of CAMGs and NGs are identical, implying that different properties for RQ MGs, NGs and CAMGs are very well possible. Consequently, there is a need to further investigate the NGs and CAMGs both experimentally and using simulation methods.

The CAMG samples are also different from both the MGs and the NG, in the following fashion: the CAMGs only partially fill a simulation box. It is important to clarify that the unfilled volume referred to is not within the film, rather it is between the upper surface of the film and the upper wall of the simulation box. The open surface at the top is expected in the CAMG film samples to give rise to surface artifacts—including defective surface coordinations, larger atomic occupancy and excess surface energy. The surface interaction between the cluster atoms and the substrate will also lead to defective coordinations at the border. It was decided to first analyze the entire CAMG film sample, and then later represent the data from a slab of fixed dimensions present within the inside of the deposited film samples, in order to avoid the surface artifacts (See Fig. S8 in Supplementary Information).

Based on the presented results, a structural model for the CAMGs is proposed, similar to that of NGs. In this model, interfacial regions, which are chemically different from the core regions due to the surface segregation observed in the individual clusters, are formed during the cluster deposition in the range of impact energies between 60 and 600 meV/atom. The only exception is, as mentioned above, the structure for an impact energy of 6000 meV/atom, for which interfaces are totally absent. Therefore, in the following sections, only simulations of CAMGs deposited at the impact energies 60, 300, and 600 meV/atom, are being considered. Incidentally, this energy range corresponds well with the energy range used in the cluster experiments reported in Ref. [24].

3.5. Structural features of CAMGs

To obtain a more detailed insight into the structure of CAMGs, in particular of the interfacial regions, the normalized pair distribution function/radial distribution function (RDF) of the CAMGs, NG, and the MGs were studied (see Fig. S9 in Supplementary Information for more details). As previously mentioned, all the six metallic glass samples (3 CAMGs, NG, MG, and MG_ht) were modelled using the interatomic potential developed by Mendelev et al. [32], which was validated by simulating $Cu_{64.5}Zr_{35.5}$ alloys. Using this potential, the Cu-Cu (2.45 Å), Cu-Zr (2.8 Å), and Zr-Zr (3.25 Å) first peak positions of the MGs match well with those previously reported values [47,48]. Even the NG and CAMGs follow the same pair distributions as those of MG. Moreover, no significant change in atomic pair correlations both in the core and the interfacial regions are observed.

In order to gain a deeper understanding of the structural differences in the six metallic glass samples, a study of the local atomic arrangements and their topology has been implemented. The local atomic arrangement or short-range order (SRO), and their contribution to the packing and, eventually, to the stability of glassy structures have been discussed in detail in previous studies. Initially, Honeycutt and Andersen [49] calculated the stability of free-standing agglomerations of 13 atoms in size—arranged in an icosahedral packing. It was later reported that the occurrence of icosahedral packing-or, full icosahedral order (FI) order—can be correlated with increased packing fraction in model metallic glasses [50]. For the case of $Cu_{64}Zr_{36}$ MGs, icosahedral atomic packing was observed to be the highest occurring structural motif [51,52]. Furthermore, for $Cu_{50}Zr_{50}$ MGs, it was observed that these FI environments were strongly spatially correlated to each other [28]. For $Cu_{50}Zr_{50}$ MGs quenched at a faster rate, less FI and icosahedral-like (ICO-like) packing or icosahedral-like order (ILO) has been found [53]. The local atomic environment is typically represented using the Voronoi analysis method [27]. This method is used to partition space and assign it to a finite set of atoms in a given region. The Voronoi polyhedra in the present analysis were determined using the methods described by Brostow et al. [54,55] and Borodin [56], and implemented on OVITO. The polyhedra are represented by a $\langle n_3\ n_4\ n_5\ n_6\rangle$ mathematical index, referred as the Schäfli notation, where n_i is the number of i-edged faces in the coordination polyhedra [57].

Fig. 4a–c show the top seven frequent Voronoi polyhedra (arranged in the numerical order of the indices) for CAMGs, NGs, MG_ht, and the precursor MG quenched at a rate of 10^{10} K/s. In Fig. 4a, the histograms of the Voronoi polyhedra for all the atoms constituting the entire six sample sets are shown, whereas Fig. 4b,c denote the histograms for the core and interface atoms, respectively. The index ⟨0 0 12 0⟩, which represents the FI coordination, is the highest occurring in the MG, amongst all the six glasses. For the 10^{10} K/s MG, the heat-treatment reduces the FI order as seen in MG_ht. The next highest occurring index is the ⟨0 2 8 2⟩, which is known to be an icosahedron-like polyhedron [53,56]. Its occurrence is highest in MG and MG_ht when compared to the NG and CAMGs. For metallic glasses in general, the Voronoi polyhedra are known to be classified into four main categories as reported by Yue et al. [53]: 1. icosahedral-like: ⟨0 0 12 0⟩, ⟨0 1 10 x⟩, and <0 2 8 *x*>; 2. crystal-like: ⟨0 4 4 x⟩ and <0 5 2 *x*>; 3. mixed coordinations: ⟨0 3 6 x⟩, where $0 \leq x \leq 4$; and 4. other remaining indices. With this knowledge, it is noticed that in the NG and CAMGs the other prominently occurring polyhedra in Fig. 4a–c are of the icosahedral-like and mixed coordination types.

Furthermore, the Voronoi indices are sorted based on the above rules for the six simulated glass samples and represented in Fig. 4d–f, in order to facilitate the analysis of the dominant indices classes in comparison of the different metallic glass structures. It is first noticed that crystalline coordinations do not occur in any of the simulated metallic glass samples, especially in the MG_ht and the CAMGs, despite the heat treatment involved in their processing. Especially, the lack of any crystalline coordinations confirms that all the simulated CAMGs are fully amorphous, both in the cores and in the interfaces.

In the CAMGs and NGs a significantly reduced short-range FI order was observed, consistent with previous studies of NGs [58]. This trend is also seen in the analysis of the ILO. The present simulations of the melt-quenched $Cu_{50}Zr_{50}$ MGs have shown that less stable MGs (prepared at higher quench rates) are accompanied by a reduction in FI fractions and also in the ILO (refer to Fi. S10 in Supplementary Information), as reported by Yue et al. [53]. Furthermore, the ILO is observed to be higher for Cu atoms than for Zr atoms for all the six metallic glass samples that have been studied (see Fig. S11 in Supplementary Information). In Fig. 4e,f it is observed that for NGs and CAMGs, both FI order and the ILO indices are respectively at least 1 and 5% higher in the interfaces compared to the cores. The interfaces, being richer in Cu compared to the core regions, exhibit higher FI as well as higher ILO. This indicates

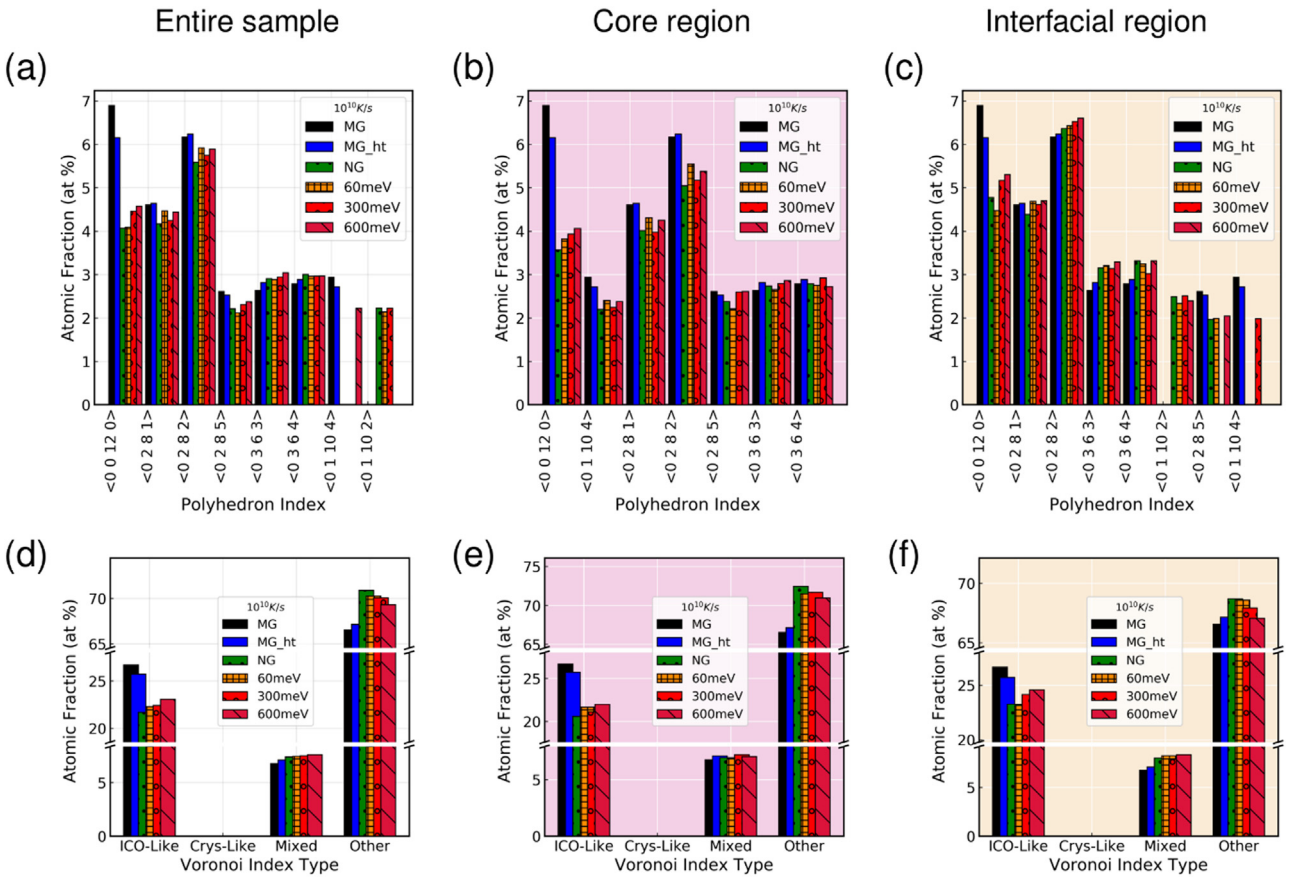

Fig. 4. The short-range order (SRO) recovers in CAMGs with deposition energy: The top 7 Voronoi indices arranged based on numerical order, without considering any special central atom species (Cu/Zr) in the Voronoi polyhedra. The Voronoi histograms are shown for (a) the entire representative sample, (b) the core atoms, and (c) the interface atoms, respectively. The magenta and yellow backgrounds in the figures are rendered to represent the core and interface cases, respectively. Fig. 4(d–f) show the indices sorted into known groups of coordinations. Crystalline coordinations are absent in all of the simulated glasses, in particular in the MG_ht, NG, and CAMGs where a heat-treatment is involved in the simulation process. The FI and ILO SRO in CAMGs increase systematically with deposition energy (See text for more details).

that the interfaces must be densely packed than the core regions. The correlation of ILO of cores and interfaces in the CAMGs and NGs, with their stability is discussed in Section 3.7.

Interestingly, a systematic increase in FI order (See Fig. 4c) in the CAMGs with increasing impact energy is observed. This trend, also seen in the ILO fractions of the entire sample, is especially prominent for the interfaces (see Fig. 4f). We recall that the interfaces are defined as the surface atoms of the undeposited clusters, and for this reason it should be noted that the interfaces for all impact energies have the same chemical composition. The increase in the FI-order and ILO in the interfacial atoms can then be interpreted to be the direct result of the CIBD process. In both the core and interface atoms, another striking feature is the systematic increase of ILO in the CAMGs with increasing deposition energy, recovering towards the ILO of MG and MG_ht. The present model demonstrates the possibility of tailoring the local amorphous order with impact energy for metallic glasses synthesized via the CIBD route.

3.6. Atomic volume distributions

The normalized distribution of the atomic coordination volumes, or Voronoi volumes [18,59] for all the atoms in the six metallic glass samples was studied using the Voronoi analysis. Fig. 5a shows the volume distribution with two peaks approximately at 13.9 $Å^3$ for Cu and 21.8 $Å^3$ for Zr, which indicates the volumes occupied by the Cu and Zr atoms. The Cu atoms are observed to have lower volume occupancies compared to those of Zr atoms. Cheng and Trelewicz [18] reported similar distributions in $Cu_{64}Zr_{36}$ nanoglasses, however, with the volume per atom peaks shifted to the left, likely caused by the fact that $Cu_{64}Zr_{36}$ MGs are denser than the $Cu_{50}Zr_{50}$ MGs [60]. Furthermore, the CAMGs are similar to the NGs and MGs in terms of atomic volume distributions. It is also noticed that the distributions in the core and in the interfaces are not significantly different from each other (see Fig. S12 in Supplementary Information). Using the volume distributions in Fig. 5a, the exclusion of the surface atoms in the analysis (mentioned in Section 3.4) of CAMGs was cross-verified. The surface atoms occupy higher volume per atom than average, and when included in the volume analysis, are known to alter the volume distributions of Cu and Zr atoms with a shoulder to the right of each main peak [18]. The absence of such shoulders indeed ascertains the absence of surface atoms in the representative Fig. 5a.

In Fig. 5b, which shows the average volume/atom values for all six metallic glass samples, it can be seen that, on average, the atoms in CAMGs and NGs occupy similar volumes. Furthermore, the impact energy does not have an influence on the average volume of the CAMGs. The core regions in the NGs and CAMGs present a higher volume occupancy. By contrast, the opposite behavior is observed for the interfacial atoms. When all of the atoms are considered together, the increase of volume for core atoms and the decrease of volume for the interface atoms in CAMGs and NGs offset each other to result in similar volume occupancies as MGs prepared by RQ. While the interfaces in NGs have previously been reported to be less dense in the MG [14,16], this need not hold true for the CAMGs as well. The interfaces are richer in Cu-

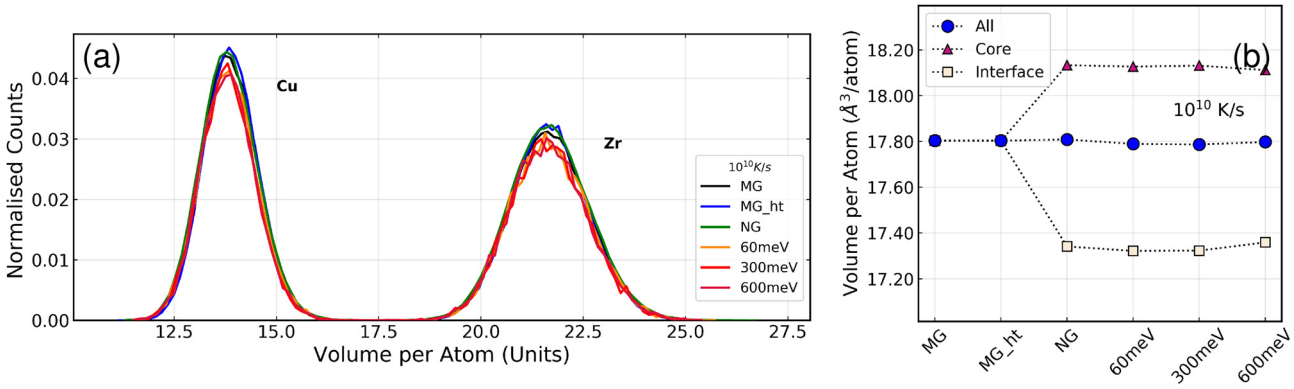

Fig. 5. Reduced volumes in cluster assembled metallic glass samples. (a) The normalized volume per atom distribution shows similar behavior for the six metallic glass samples. (b) Average volumes of the atoms show that the core regions are less densely packed than the interfaces.

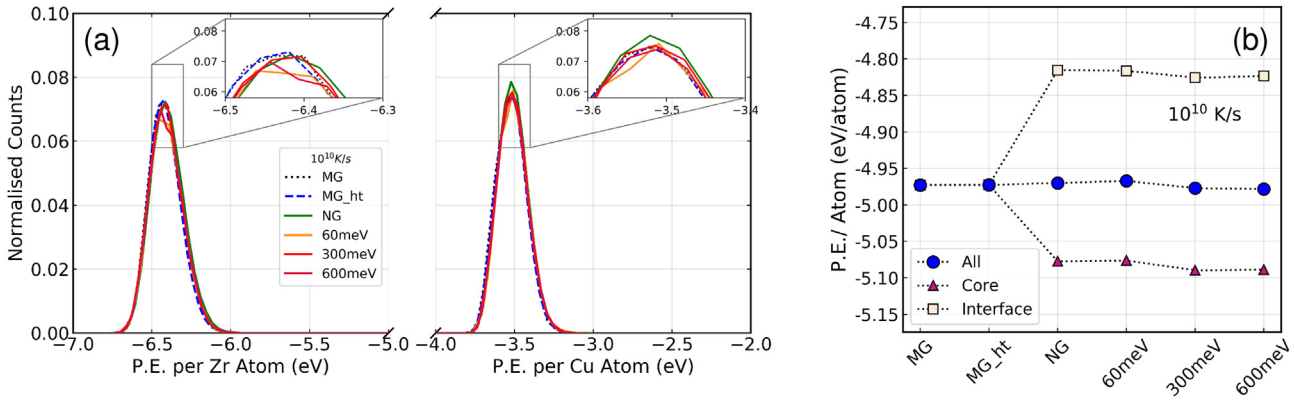

Fig. 6. Potential energy states of the CAMGs, NG and MGs. (a) The normalized potential energy distributions for the six glasses. (b) The average potential energy per atom, also in the core and interface regions for all the glasses.

atoms, which, on an average, occupy lower volumes compared to Zr-atoms. The interfaces in the present CAMGs model have an increased density due to the chemical effects, and this is consistent with previous studies of segregated planar interfaces by Adjaoud and Albe [29].

3.7. Potential energy distributions

In Fig. 6a, the normalized potential energy distribution of the simulated CAMGs, NG and MGs are summarized. The Cu and Zr atoms exhibit two separate distributions, with the peaks of −3.5 eV for Cu atoms and −6.5 eV for Zr atoms. By contrast to the atomic volume distribution behavior, where the Cu atoms occupied lower volumes, the Cu atoms have a higher potential energy overall in comparison to Zr atoms. The absence of right shoulders in the potential energy distribution peaks, like in the volume distributions discussed in Section 3.6, once again confirms the absence of surface atoms in the representative CAMG slabs.

Fig. 6b summarizes the average potential energies for all atoms in the MG, MG_ht, NG, and the CAMGs and the average potential energies of the atoms in the core and interfacial regions in the NG and CAMGs, deposited at the different impact energies. All of these six metallic glasses samples have been made from a 10^{10} K/s $Cu_{50}Zr_{50}$ glass. It is observed that the core and interfacial atoms in the CAMGs and NGs can be distinguished by their energetic states. The core atoms occupy lower energy states, about 2% lower than that of the atoms in MGs prepared by RQ, whereas the interfaces possess higher energies ∼6% higher compared to those of the MGs. While the interfaces are better packed than the cores, as seen in Section 3.6, they occupy a higher energy state than the MGs. From liquid quenched traditional metallic glasses it is known that the total potential energy of the glass increases with increasing Cu concentration maintaining the same quenching rate (see Fig. S13 in Supplementary Information). Hence, it can be explained that the higher Cu concentration in the interfaces, results in the interface atoms residing at a higher energy state. We conclude that the core regions stabilize the CAMGs and the NGs. Denser packing at the interfaces does not necessarily correspond to a lower energy state in the NGs and CAMGs due to their chemical heterogeneity.

In the following section, the medium-range order (MRO) in all six metallic glasses (3 CAMGs, NG, MG and MG_ht) will be inspected to better understand the connectivity of the FI units in the MG and MG_ht and how the MRO varies in the CAMGs with the deposition energy.

3.8. Medium-range order in CAMGs

The relative packing of coordination polyhedra centered around solute atoms is used to define MRO in metallic glasses; it has been shown that the solute atoms exhibit string-like connectivity when the solute concentration goes beyond 20–30 at.%, [27]. Similarly, the string-like connectivity of FI-atoms, which are the atoms residing in FI coordinations, have been reported to indicate MRO, as icosahedral ⟨0 0 12 0⟩ clusters have a strong tendency to aggregate with each other [27,28,61]. Interpenetrating string-like networks of atoms in FI environments have been reported before as indicative of MRO, including studies by Lee et al. [62] and by Ritter et al. [63]. To visualize these strings for the glasses simulated in this work,

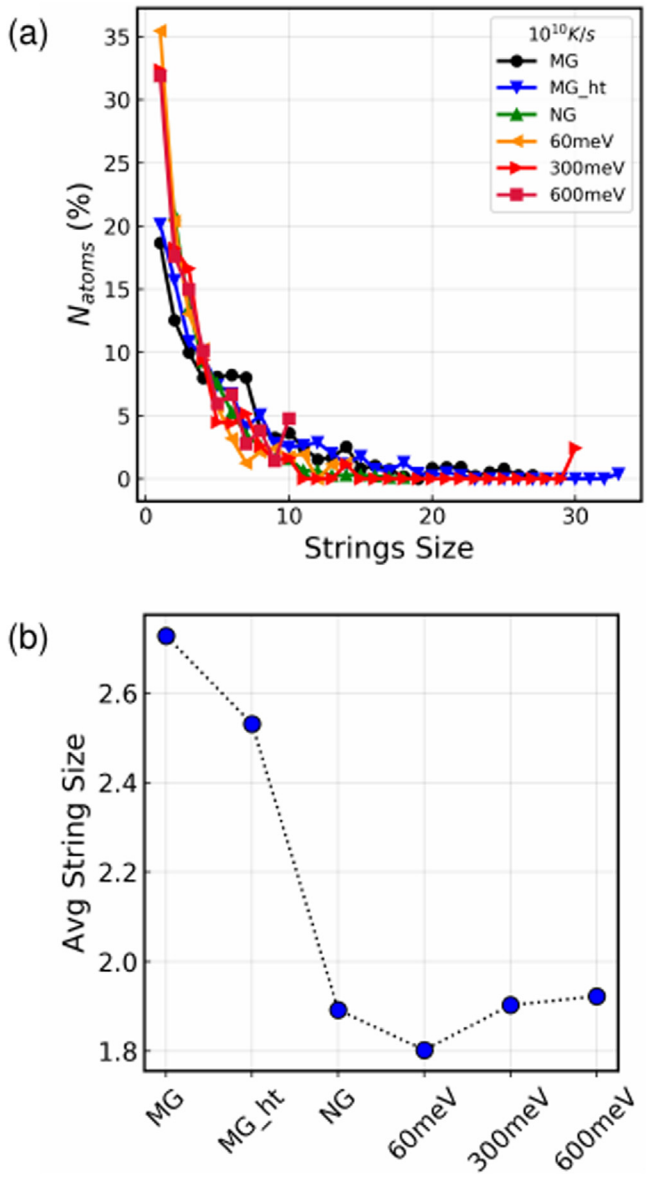

Fig. 7. Medium range order (MRO) recovers in CAMGs with deposition energy. (a) The fraction of FI-atoms occurring in a string of a given size, and (b) the average string size in the glass samples as function of the deposition energy.

bonds were constructed for FI-atoms with other FI-atoms, present within a cut-off radius of 3.5 Å.

Fig. 7a shows the fraction of FI-atoms in each of the glasses made from a 10^{10} K/s MG, which are present in a string of a given size. From the figure, it is evident that most FI-atoms exist in small strings. However, the number of atoms in small strings (3–5 FI-atoms in size) is the lowest in the MG and MG_ht. A higher percentage of larger-sized strings is seen in the MG, MG_ht and NG. This can be attributed to the geometry of the samples: larger strings can form in MG, MG_ht, and NG cases due to periodic boundaries conditions in all directions, and the simulation box being completely filled. Such strings of larger sizes cannot be expected to form in the CAMGs, as the sample considered for analysis without surface artifacts is limited by the dimensions of the representative slabs from within the CAMG films. However, amongst the 3 CAMGs, it can still be noted that a 600 meV/atom CAMG has more 3 FI-atom strings than the 60 meV/atom CAMG. This trend is seen for strings of at least 5 FI-atoms in length. Fig. 7b shows the average string size for all simulated glasses. The average string size in NG and CAMGs is about 40% lower than for MG and MG_ht. However, with increasing deposition energy, a slight increase in average string size in the CAMGs deposited at 60 and 300 meV/atom compared to the 60 meV/atom CAMG is observed. This indicates that with increasing deposition energies in the CAMGs, the MRO of the strings of FI-atoms can be at least partially recovered. A comparison of the present results with the available experimental data including the structural and magnetic information on $Fe_{80}Sc_{20}$ CAMGs is not possible as the current simulations are specific to the $Cu_{50}Zr_{50}$ metallic glass, and also due to the non-availability of an EAM potential for $Fe_{80}Sc_{20}$ systems. However, some conclusions on the behavior of cluster-assembled glasses, in particular on the of the medium-range order in CAMGs, can help to better understand the experimental results for $Fe_{80}Sc_{20}$ CAMGs, in particular the comparison to the local motif analysis reported in [24]. As the local order in CAMGs recovers towards the metallic glass values with increasing impact energies, an increase in the size of the string-like MRO networks is expected. This behavior could explain the strengthening of exchange interactions, and thus the observed increase in the ferromagnetic transition temperature (Curie temperature) with increasing impact energy.

Next, in Section 3.9, an attempt is made to explain the dependence of the final metastable states of the NG and CAMGs on the initial processing conditions of the clusters themselves. This could help to understand the CIBD process and would allow to traverse the potential-energy landscape (PEL) of metallic glasses. One important processing condition in the simulation is the quenching rate of the MG from which the clusters are formed. Therefore, a comparison of CAMGs and NGs, prepared with different quenching rates is made.

3.9. Influence of quenching rate on the final structure of NGs and CAMGs

In the previous sections, it has been mentioned that the ILO is a well-known indicator of glass stability and of packing [51–53,64]. Now, the ILO behavior in CAMGs is observed with respect to the processing conditions of the RQ MGs, from which the clusters are derived. CAMGs made from fast-quenched 10^{12} K/s-MGs and 10^{12} K/s-MGs were investigated. Fig. 8 shows the variation of the ILO for three different quenching rates from which the clusters were prepared. Firstly, it can be seen that the ILO of the MG decreases with increasing quenching rates. Secondly, the heat-treatment for the MGs results in different dependence for the different quenching rates. For the MGs prepared with cooling rates 10^{10} and 10^{12} K/s (Fig. 8a,b), the heat-treated glasses MG_ht exhibit lower ILO than the MG. At the highest cooling rate of 10^{14} K/s, the same heat-treatment places the MG_ht at a state with higher ILO value (Fig. 8c). Given that the clusters undergo the same heat-treatment as MG_ht, the NGs and CAMGs can be compared with the MG_ht.

For the NG and CAMGs, across the three quenching rates, the ILO is lesser in comparison to their respective MG_ht. At all quenching rates, it is noted that the interfaces exhibit higher SRO than the cores, due to the chemical effects discussed in Section 3.5. The CAMGs, however, show an increase in the ILO with increasing impact energies, for all the three quench rates used in the present study. Therefore, it is concluded that for a given cooling rate of the as-prepared clusters, the CIBD process determines the final states of the CAMGs.

Unlike in the MG and the MG_ht, the ILO packing and stability do not correlate with each other in the CAMGs and NGs. For a CAMG prepared at a given impact energy, the ILO packing increases with quenching rate. The strain energy due to CAMG processing could be dominating the stability gained from the slow quench-

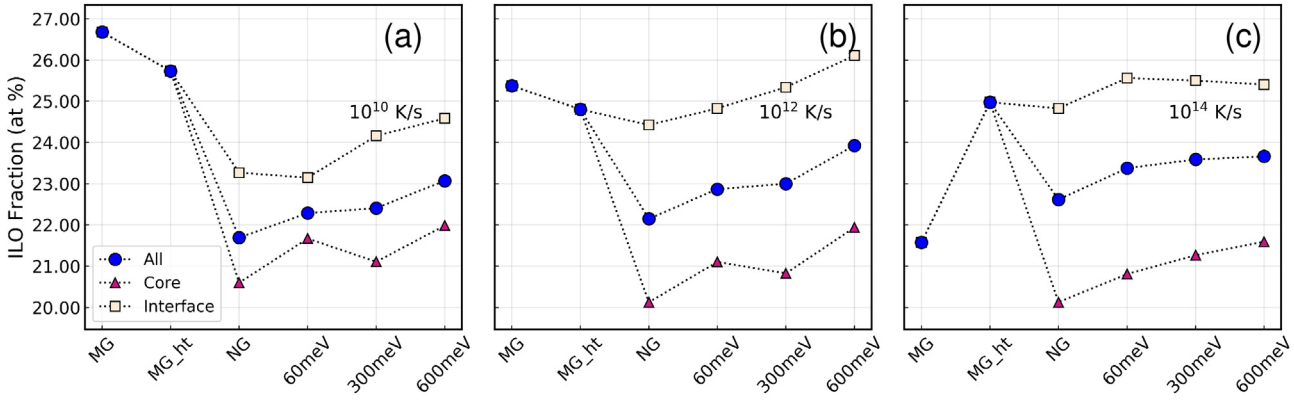

Fig. 8. Icosahedral-like ordering versus quench rates. Variation of ILO in the various CAMGs and MGs, compared to their precursor MGs and MG_ht s for cluster derived from (a) 10^{10} K/s, (b) 10^{12} K/s, and (c) 10^{14} K/s $Cu_{50}Zr_{50}$ MGs.

ing rate in the NGs and CAMGs, leading to the observed behavior. In Fig. 3d, the strain analysis shows that von-Mises strains for the 3 nm clusters studied here are higher in both NGs and CAMGs, compared to previous reports for 7 nm cluster NGs [17]. This leads to the conclusion that the size of the clusters plays an important role in the final structures attained by the CAMGs. Further studies with different cluster sizes, including size distributions, and random deposition locations are needed to gain further understanding on the role of the processing parameters in cluster assembled metallic glasses prepared by compaction (NGs) and by energetic impact (CAMGs).

4. Conclusions

In this study, a molecular dynamics simulation protocol was developed to study the local structure of $Cu_{50}Zr_{50}$ cluster-assembled metallic glasses (CAMGs). The present model of CAMGs uses chemically segregated amorphous $Cu_{50}Zr_{50}$ clusters of ~800 atoms, which are 3 nm in diameter, being deposited onto a substrate at different impact energies. These CAMGs are compared with NGs produced by mechanical compaction of the same precursor clusters, and to the conventionally prepared melt-quenched metallic glasses of the same composition. The main results of the study are as follows:

(1) In the CAMGs, two chemically distinct amorphous phases were observed: cores and interfaces, which constitute an interconnected network of interfaces in which the cores with their distinctly different local structure are embedded. The formation of Cu-rich interfaces is observed at impact energies up to 600 meV/atom. The interfaces appear to be completely absent at the extreme impact energy of 6000 meV/atom.
(2) The FI and ILO short-range order parameters in the conventional (10^{10} K/s quench rate) case, are lower in the NG and CAMG, compared to the RQ MG, in both the cores and interfaces. The interfaces exhibit higher FI and ILO compared to the cores, with a higher density than the cores. Due to the chemical heterogeneity between cores and interfaces, the core regions occupy lower energy states, thus stabilizing the CAMG structures.
(3) The local ILO as well as the MRO in CAMGs are found to increase with the impact energy. Furthermore, the ILO increases with impact energy, irrespective of the quenching rates used to prepare the clusters. Consequently, at a fixed overall bulk composition of the metallic glass, control of the local structure is possible by modifying the processing conditions. The SRO and MRO in CAMGs recover towards the metallic glass values with increasing impact energies.

Declaration of Competing Interest

The authors declare that they have no known competing financial interests or personal relationships that could have appeared to influence the work reported in this paper.

Acknowledgments

SPC thanks the supercomputer ForHLR II (funded by the Ministry of Science, Research and the Arts Baden-Württemberg and by the Federal Ministry of Education and Research) for funding. HH appreciates many fruitful discussions with Herbert Gleiter over the years on the subject of nanoglasses and cluster-assembled materials.

Supplementary materials

Supplementary material associated with this article can be found, in the online version, at doi:10.1016/j.actamat.2022.118152 studies.

References

[1] W. Klement, R.H. Willens, P. Duwez, Non-crystalline Structure in solidified gold-silicon alloys, Nature 187 (1960) 869–870, doi:10.1038/187869b0.
[2] A.W. Weeber, H. Bakker, Amorphization by ball milling. A review, Phys. B Phys. Condens. Matter 153 (1988) 93–135, doi:10.1016/0921-4526(88)90038-5.
[3] A.L. Greer, Metallic glasses, Science 267 (1979) 1947–1953 1995, doi:10.1126/science.267.5206.1947.
[4] L. Berthier, M.D. Ediger, Facets of glass physics, Phys. Today 69 (2016) 40–46, doi:10.1063/PT.3.3052.
[5] C. Suryanarayana, Mechanical alloying and milling, Prog. Mater. Sci. 46 (2001) 1–184, doi:10.1016/S0079-6425(99)00010-9.
[6] M.M. Trexler, N.N. Thadhani, Mechanical properties of bulk metallic glasses, Prog. Mater. Sci. 55 (2010) 759–839, doi:10.1016/j.pmatsci.2010.04.002.
[7] J. Jing, A. Krämer, R. Birringer, H. Gleiter, U. Gonser, Modified atomic structure in a PdFeSi nanoglass. A Mössbauer study, J. Non Cryst. Solids 113 (1989) 167–170, doi:10.1016/0022-3093(89)90007-0.
[8] H. Gleiter, T. Schimmel, H. Hahn, Nanostructured solids - from nano-glasses to quantum transistors, Nano Today 9 (2014) 17–68, doi:10.1016/j.nantod.2014.02.008.
[9] Y. Ivanisenko, C. Kübel, S.H. Nandam, C. Wang, X. Mu, O. Adjaoud, K. Albe, H. Hahn, Structure and properties of nanoglasses, Adv. Eng. Mater. 20 (2018) 1800404, doi:10.1002/adem.201800404.
[10] J.X. Fang, U. Vainio, W. Puff, R. Würschum, X.L. Wang, D. Wang, M. Ghafari, F. Jiang, J. Sun, H. Hahn, H. Gleiter, Atomic structure and structural stability of Sc_{75} Fe_{25} nanoglasses, Nano Lett. 12 (2012) 458–463, doi:10.1021/nl2038216.
[11] M. Ghafari, H. Hahn, H. Gleiter, Y. Sakurai, M. Itou, S. Kamali, Evidence of itinerant magnetism in a metallic nanoglass, Appl. Phys. Lett. 101 (2012), doi:10.1063/1.4769816.

[12] J. Weissmüller, R. Birringer, H. Gleiter, Nanostructured crystalline and amorphous solids, Key Eng. Mater. 77-78 (1992) 161–170, doi:10.4028/www.scientific.net/kem.77-78.161.

[13] H. Gleiter, Nanoglasses: a new kind of noncrystalline material and the way to an age of new technologies? Small 12 (2016) 2225–2233, doi:10.1002/smll.201500899.

[14] R. Witte, T. Feng, J.X. Fang, A. Fischer, M. Ghafari, R. Kruk, R.A. Brand, D. Wang, H. Hahn, H. Gleiter, Evidence for enhanced ferromagnetism in an iron-based nanoglass, Appl. Phys. Lett. 103 (2013), doi:10.1063/1.4818493.

[15] S.H. Nandam, Y. Ivanisenko, R. Schwaiger, Z. Śniadecki, X. Mu, D. Wang, R. Chellali, T. Boll, A. Kilmametov, T. Bergfeldt, H. Gleiter, H. Hahn, Cu-Zr nanoglasses: atomic structure, thermal stability and indentation properties, Acta Mater. 136 (2017) 181–189, doi:10.1016/j.actamat.2017.07.001.

[16] D. Şopu, K. Albe, Y. Ritter, H. Gleiter, From nanoglasses to bulk massive glasses, Appl. Phys. Lett. 94 (2009), doi:10.1063/1.3130209.

[17] O. Adjaoud, K. Albe, Microstructure formation of metallic nanoglasses: insights from molecular dynamics simulations, Acta Mater. 145 (2018) 322–330, doi:10.1016/j.actamat.2017.12.014.

[18] B. Cheng, J.R. Trelewicz, Controlling interface structure in nanoglasses produced through hydrostatic compression of amorphous nanoparticles, Phys. Rev. Mater. 3 (2019) 1–9, doi:10.1103/PhysRevMaterials.3.035602.

[19] S.H. Nandam, R. Schwaiger, A. Kobler, C. Kübel, C. Wang, Y. Ivanisenko, H. Hahn, Controlling shear band instability by nanoscale heterogeneities in metallic nanoglasses, J. Mater. Res. 36 (2021) 2903–2914, doi:10.1557/s43578-021-00285-4.

[20] S.H. Nandam, O. Adjaoud, R. Schwaiger, Y. Ivanisenko, M.R. Chellali, D. Wang, K. Albe, H. Hahn, Influence of topological structure and chemical segregation on the thermal and mechanical properties of Pd-Si nanoglasses, Acta Mater. 193 (2020) 252–260, doi:10.1016/j.actamat.2020.03.021.

[21] A. Kartouzian, Cluster-assembled metallic glasses, Nanoscale Res. Lett. 8 (2013) 2–5.

[22] A. Kartouzian, J. Antonowicz, T. Lünskens, A. Lagogianni, P. Heister, G. Evangelakis, R. Felici, Toward cluster-assembled metallic glasses, Mater. Express 4 (2014) 228–234, doi:10.1166/mex.2014.1168.

[23] C. Benel, T. Reisinger, R. Kruk, H. Hahn, Cluster-assembled nanocomposites: functional properties by design, Adv. Mater. 31 (2019) 1806634, doi:10.1002/adma.201806634.

[24] C. Benel, A. Fischer, A. Zimina, R. Steininger, R. Kruk, H. Hahn, A. Léon, Controlling the structure and magnetic properties of cluster-assembled metallic glasses, Mater. Horiz. 6 (2019) 727–732, doi:10.1039/c8mh01013g.

[25] J.D. Bernal, A geometrical approach to the structure Of liquids, Nature 183 (1959) 141–147, doi:10.1038/183141a0.

[26] D.B. Miracle, A structural model for metallic glasses, Nat. Mater. 3 (2004) 697–702, doi:10.1038/nmat1219.

[27] H.W. Sheng, W.K. Luo, F.M. Alamgir, J.M. Bai, E. Ma, Atomic packing and short-to-medium-range order in metallic glasses, Nature 439 (2006) 419–425, doi:10.1038/nature04421.

[28] H.L. Peng, M.Z. Li, W.H. Wang, C.Z. Wang, K.M. Ho, Effect of local structures and atomic packing on glass forming ability in Cu_xZr_{100-x} metallic glasses, Appl. Phys. Lett. 96 (2010) 2008–2011, doi:10.1063/1.3282800.

[29] O. Adjaoud, K. Albe, Interfaces and interphases in nanoglasses: surface segregation effects and their implications on structural properties, Acta Mater. 113 (2016) 284–292, doi:10.1016/j.actamat.2016.05.002.

[30] S. Plimpton, Fast parallel algorithms for short-range molecular dynamics, J. Comput. Phys. 117 (1995) 1–19, doi:10.1006/jcph.1995.1039.

[31] A.P. Thompson, H.M. Aktulga, R. Berger, D.S. Bolintineanu, W.M. Brown, P.S. Crozier, P.J. in 't Veld, A. Kohlmeyer, S.G. Moore, T.D. Nguyen, R. Shan, M.J. Stevens, J. Tranchida, C. Trott, S.J. Plimpton, LAMMPS - a flexible simulation tool for particle-based materials modeling at the atomic, meso, and continuum scales, Comput. Phys. Commun. 271 (2022) 108171, doi:10.1016/j.cpc.2021.108171.

[32] M.I. Mendelev, Y. Sun, F. Zhang, C.Z. Wang, K.M. Ho, Development of a semi-empirical potential suitable for molecular dynamics simulation of vitrification in Cu-Zr alloys, J. Chem. Phys. 151 (2019), doi:10.1063/1.5131500.

[33] M.S. Daw, S.M. Foiles, M.I. Baskes, The embedded-atom method: a review of theory and applications, Mater. Sci. Rep. 9 (1993) 251–310, doi:10.1016/0920-2307(93)90001-U.

[34] A. Stukowski, Visualization and analysis of atomistic simulation data with OVITO-the open visualization tool, Model. Simul. Mater. Sci. Eng. 18 (2010), doi:10.1088/0965-0393/18/1/015012.

[35] S. Plimpton, M. Jones, Pizza.py Toolkit, 2020, (n.d.). https://lammps.github.io/pizza/open_source.html.

[36] A. Fischer, R. Kruk, H. Hahn, A versatile apparatus for the fine-tuned synthesis of cluster-based materials, Rev. Sci. Instrum. 86 (2015), doi:10.1063/1.4908166.

[37] H. Haberland, Z. Insepov, M. Moseler, Molecular dynamics simulation of thin film formation by energetic cluster impact (ECI), Z. Phys. D Atoms, Mol. Clust. 26 (1993) 229–231, doi:10.1007/BF01429153.

[38] H. Haberland, Z. Insepov, M. Moseler, Molecular-dynamics simulation of thin-film growth by energetic cluster impact, Phys. Rev. B 51 (1995) 11061–11067, doi:10.1103/PhysRevB.51.11061.

[39] S. Rahmati, A. Zúñiga, B. Jodoin, R.G.A. Veiga, Deformation of copper particles upon impact: a molecular dynamics study of cold spray, Comput. Mater. Sci. 171 (2020) 109219, doi:10.1016/j.commatsci.2019.109219.

[40] P. Meakin, P. Ramanlal, L.M. Sander, R.C. Ball, Ballistic deposition on surfaces, Phys. Rev. A 34 (1986) 5091–5103, doi:10.1103/PhysRevA.34.5091.

[41] C. Kalcher, O. Adjaoud, J. Rohrer, A. Stukowski, K. Albe, Reinforcement of nanoglasses by interface strengthening, Scr. Mater. 141 (2017) 115–119, doi:10.1016/j.scriptamat.2017.08.004.

[42] B. Cheng, J.R. Trelewicz, Interfacial plasticity governs strain delocalization in metallic nanoglasses, J. Mater. Res. 34 (2019) 2325–2336, doi:10.1557/jmr.2019.101.

[43] K. Zheng, S. Yuan, H. Hahn, P.S. Branicio, Excess free volume and structural properties of inert gas condensation synthesized nanoparticles based CuZr nanoglasses, Sci. Rep. 11 (2021) 1–11, doi:10.1038/s41598-021-98494-8.

[44] A. Stukowski, Computational analysis methods in atomistic modeling of crystals, JOM 66 (2014) 399–407, doi:10.1007/s11837-013-0827-5.

[45] Y.Q. Cheng, A.J. Cao, E. Ma, Correlation between the elastic modulus and the intrinsic plastic behavior of metallic glasses: the roles of atomic configuration and alloy composition, Acta Mater. 57 (2009) 3253–3267, doi:10.1016/j.actamat.2009.03.027.

[46] H. Gleiter, Nanocrystalline solids, J. Appl. Crystallogr. 24 (1991) 79–90, doi:10.1107/S0021889890011013.

[47] T. Nasu, S. Takahashi, I. Ajiki, T. Usuki, Y. Onodera, M. Sakurai, Z. Wei, A. Inoue, B. He, W. Zhong, Z. Xie, S. Wei, Direct observation of the changes in atomic arrangement of $Cu_{50}Zr_{50}$ metallic glass during tensile deformation by EXAFS, J. Alloy. Compd. 434-435 (2007) 44–47, doi:10.1016/j.jallcom.2006.08.115.

[48] G. Duan, D. Xu, Q. Zhang, G. Zhang, T. Cagin, W.L. Johnson, W.A. Goddard, Molecular dynamics study of the binary $Cu_{46}Zr_{54}$ metallic glass motivated by experiments: glass formation and atomic-level structure, Phys. Rev. B Condens. Matter Mater. Phys. 71 (2005) 1–9, doi:10.1103/PhysRevB.71.224208.

[49] J.D. Honeycutt, H.C. Andersen, Molecular dynamics study of melting and freezing of small Lennard-Jones clusters, J. Phys. Chem. 91 (1987) 4950–4963, doi:10.1021/j100303a014.

[50] A.S. Clarke, H. Jónsson, Structural changes accompanying densification of random hard-sphere packings, Phys. Rev. E 47 (1993) 3975–3984, doi:10.1103/PhysRevE.47.3975.

[51] J. Ding, Y.Q. Cheng, E. Ma, Full icosahedra dominate local order in $Cu_{64}Zr_{34}$ metallic glass and supercooled liquid, Acta Mater. 69 (2014) 343–354, doi:10.1016/j.actamat.2014.02.005.

[52] J. Ding, S. Patinet, M.L. Falk, Y. Cheng, E. Ma, Soft spots and their structural signature in a metallic glass, Proc. Natl. Acad. Sci. USA 111 (2014) 14052–14056, doi:10.1073/pnas.1412095111.

[53] X.X. Yue, C.T. Liu, S.Y. Pan, A. Inoue, P.K. Liaw, C. Fan, Effect of cooling rate on structures and mechanical behavior of $Cu_{50}Zr_{50}$ metallic glass: a molecular-dynamics study, Phys. B 547 (2018) 48–54, doi:10.1016/j.physb.2018.07.030.

[54] W. Brostow, M. Chybicki, R. Laskowski, J. Rybicki, Voronoi polyhedra and Delaunay simplexes in the structural analysis of molecular-dynamics-simulated materials, Phys. Rev. B Condens. Matter Mater. Phys. 57 (1998) 13448–13458, doi:10.1103/PhysRevB.57.13448.

[55] W. Brostow, J.P. Dussault, B.L. Fox, Construction of Voronoi polyhedra, J. Comput. Phys. 29 (1978) 81–92, doi:10.1016/0021-9991(78)90110-9.

[56] V.A. Borodin, Local atomic arrangements in polytetrahedral materials, Philos. Mag. A 79 (1999) 1887–1907 physics of Condensed Matter, Structure, Defects and Mechanical Properties, doi:10.1080/01418619908210398.

[57] H.S.M. Coxeter, Regular Polytopes, 3rd ed., Dover Publications, 1973 https://www.amazon.com/Regular-Polytopes-H-S-Coxeter/dp/0486614808.

[58] O. Adjaoud, K. Albe, Influence of microstructural features on the plastic deformation behavior of metallic nanoglasses, Acta Mater. 168 (2019) 393–400, doi:10.1016/j.actamat.2019.02.033.

[59] B.F. Lu, L.T. Kong, K.J. Laws, W.Q. Xu, Z. Jiang, Y.Y. Huang, M. Ferry, J.F. Li, Y.H. Zhou, EXAFS and molecular dynamics simulation studies of Cu-Zr metallic glass: short-to-medium range order and glass forming ability, Mater. Charact. 141 (2018) 41–48, doi:10.1016/j.matchar.2018.04.036.

[60] Y. Li, Q. Guo, J.A. Kalb, C.v. Thompson, Matching glass-forming ability with the density of the amorphous phase, Science 322 (1979) 1816–1819 2008, doi:10.1126/science.1163062.

[61] M. Li, C.Z. Wang, S.G. Hao, M.J. Kramer, K.M. Ho, Structural heterogeneity and medium-range order in Zr_xCu_{100-x} metallic glasses, Phys. Rev. B Condens. Matter Mater. Phys. 80 (2009) 1–7, doi:10.1103/PhysRevB.80.184201.

[62] M. Lee, C.M. Lee, K.R. Lee, E. Ma, J.C. Lee, Networked interpenetrating connections of icosahedra: effects on shear transformations in metallic glass, Acta Mater. 59 (2011) 159–170, doi:10.1016/j.actamat.2010.09.020.

[63] Y. Ritter, D. Sopu, H. Gleiter, K. Albe, Structure, stability and mechanical properties of internal interfaces in $Cu_{64}Zr_{36}$ nanoglasses studied by MD simulations, Acta Mater. 59 (2011) 6588–6593, doi:10.1016/j.actamat.2011.07.013.

[64] Y.Q. Cheng, H.W. Sheng, E. Ma, Relationship between structure, dynamics, and mechanical properties in metallic glass-forming alloys, Phys. Rev. B Condens. Matter Mater. Phys. 78 (2008) 1–7, doi:10.1103/PhysRevB.78.014207.